NDT
Journal of Non-Destructive Testing

MDPI

Article

Angle Modulation Phase Shift in Vibro-Acoustic Modulation: A Novel Approach for Early Crack Detection

Mohammad M. Bazrafkan [1,*], Norbert Hoffmann [2] and Marcus Rutner [1,*]

[1] Institute for Metal and Composite Structures, Hamburg University of Technology, Denickestr. 17, 21073 Hamburg, Germany
[2] Institute for Structural Dynamics, Hamburg University of Technology, Schloßmühlendamm 30, 21073 Hamburg, Germany; norbert.hoffmann@tuhh.de
* Correspondence: mohammad.bazrafkan@tuhh.de (M.M.B.); marcus.rutner@tuhh.de (M.R.); Tel.: +49-(0)40-42878-3222 (M.M.B.); +49-(0)40-42878-3022 (M.R.)

Abstract

Detecting structural defects is one of the primary challenges engineers face. Consequently, the development of techniques and methods capable of detecting structural defects has always been critical. It should be emphasized that crack detection is only meaningful if it occurs before the final stages of structural failure. Accordingly, the early identification of structural defects has become a significant research challenge, motivating the development of techniques and diagnostic parameters that can effectively capture and reflect the structure's nonlinearity or non-uniform behavior. This study aims to provide a more detailed examination of modulation phenomena observed in the measured response using the vibro-acoustic modulation (VAM) method, and propose a new model that simultaneously incorporates all three conventional modulation types (amplitude, frequency, and phase), which may offer a more accurate representation of the response signal behavior. Both theoretical and experimental results clearly confirm that the phase shifts of individual frequency components in the frequency domain vary throughout the lifetime of the tested specimen. This behavior, as anticipated by the proposed model, reveals a strong correlation between phase shifts and modulation indices (MIs). Furthermore, the relative sensitivity analysis indicates that the phase shift is more sensitive than the modulation index (MI), suggesting its strong potential as an indicator for early defect detection in structural components.

Keywords: vibroacoustic; modulation index; phase shift; early detection; relative sensitivity

Academic Editor: Fabio Tosti

Received: 6 December 2025
Revised: 6 January 2026
Accepted: 7 January 2026
Published: 9 January 2026

1. Introduction

Early detection of defects in structures has emerged as a key research challenge in Structural Health Monitoring (SHM) and non-destructive evaluation (NDE). To this end, the system under test is analyzed to identify one or more diagnostic parameters that distinguish between the healthy and faulty states of the structure. Vibro-Acoustic Modulation (VAM) is a nonlinear ultrasonic technique used in NDE and SHM to detect and characterize damage in a wide range of materials and structural components.

Vibro-Acoustic Modulation (VAM) method, first introduced by Donskoy and Sutin in 1998 [1,2]. In this method, two signals at low (Ω) and high (ω) frequencies, which are called X_Ω and X_ω as represented in Equation (1), are simultaneously excited to a structure under test (SUT), and another sensor (or sensors) measures a response signal, simultaneously. Furthermore, VAM also shows potential for crack localization [3–7], as first proposed theoretically by Donskoy [2] but not further explored experimentally.

The behavior of the SUT can be described in two different situations: (1) When the structure is perfectly elastic and defect-free, its stress–strain relationship is well-approximated by a linear Hookean law $\sigma(\varepsilon) = E\,\varepsilon$, where σ, ε, and E represent stress, strain, and Young's Modulus, respectively. Under this condition X_Ω and X_ω do not significantly interact, and no sidebands are generated [1,2]. The frequency response of the measured signal reveals only frequency components at ω and Ω, as shown in Figure 1b.

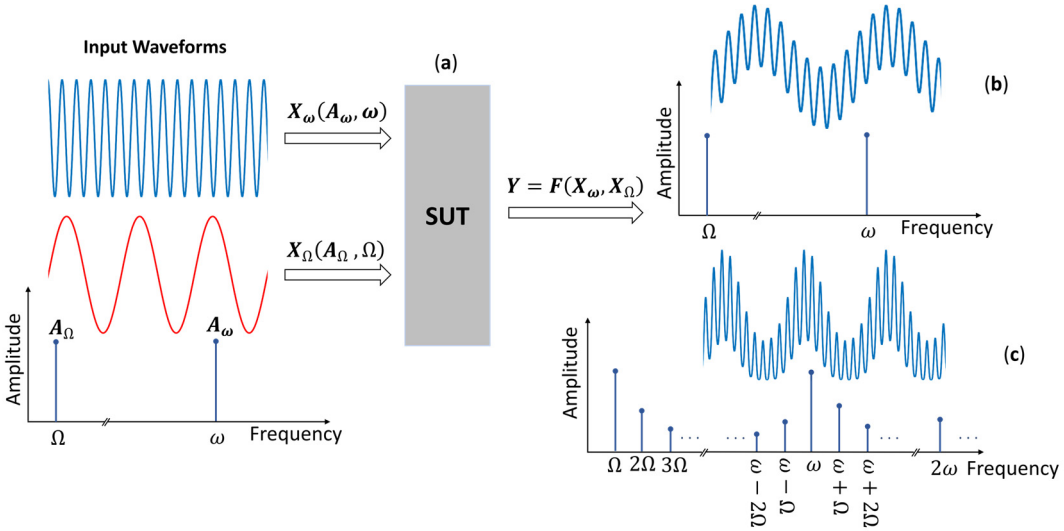

Figure 1. The fundamentals of the Vibro-Acoustic Modulation method—(**a**) a test setup, (**b**) the frequency component of the response, when SUT has no defect, and (**c**) when SUT has a defect.

(2) When the structure has a defect such as a crack, the defect introduces a localized **nonlinear** stress–strain behavior. A simple nonlinear stress–strain can be written using a polynomial expansion, $\sigma(\varepsilon) = E\,\varepsilon + \alpha\,\varepsilon^2 + \beta\,\varepsilon^3 + \cdots$, where α and β are higher-order nonlinear coefficients related to microstructural or contact-type nonlinearity. Under this condition, the high-order polynomial terms in the nonlinear stress–strain expansion generate higher harmonics of X_Ω and X_ω and the sidebands at $\omega \pm n\Omega$ [1,2,8–12]. The frequency response of the measured signal in this condition reveals frequency components not only at ω and Ω, but higher harmonics of ω and Ω as well as $\omega \pm n\Omega$, as shown in Figure 1c.

$$\begin{aligned} &\text{LF signal}: \quad X_\Omega(t) \equiv X_\Omega(A_\Omega, \Omega) = A_\Omega Cos(\Omega t + \theta_\Omega)\,,\ \Omega = 2\pi f_\Omega \quad \text{a} \\ &\text{HF signal}: \quad X_\omega(t) \equiv X_\omega(A_\omega, \omega) = A_\omega Cos(\omega t + \theta_\omega),\ \omega = 2\pi f_\omega \quad \text{b} \end{aligned} \tag{1}$$

Donskoy et al. [13] discussed the nonlinear interaction between ultrasonic waves and low-frequency vibrations at contact interfaces containing defects, such as cracks and delamination, using the VAM technique. By modulating an HF ultrasonic wave with LF vibrations, defect-induced signals can be distinguished from linear acoustic reflections, allowing more sensitive detection. Their results demonstrate how observing sideband components enhances defect identification and may provide insights into defect size and bonding strength.

Duffour et al. [14] examine the effectiveness of VAM for crack detection in metals, focusing on the amplitude modulation of ultrasonic waves (HF signal) by LF vibrations. The authors investigated the relationship between crack size and modulation strength, noting that the correlation is poor due to the sensitivity of the technique to initial crack states and setup conditions.

In another work, Donskoy [15] emphasized that linear methods often miss tiny damages in structures. Nonlinear methods, including harmonic distortion and modulation

techniques, exploit stress–strain nonlinearities that become more pronounced in the vicinity of defects such as cracks or delamination.

Aymerich and Staszewski [16] explored cross-modulation vibro-acoustic techniques for detecting impact damage in composite laminates. A slow, amplitude-modulated pumping wave is paired with a constant-amplitude probing wave, producing modulation effects that indicate the presence of damage. The study demonstrated how sidebands in the power spectrum of the probing wave correlate with the severity of barely visible impact damage. Despite boundary condition challenges, the authors validate the flexibility and effectiveness of the technique for early-stage damage detection.

In 2010, Hu et al. [17] investigated nonlinear VAM for crack detection using piezoceramic transducers, focusing on separating amplitude and frequency modulations via the Hilbert–Huang transform (HHT). Their findings show that amplitude modulation correlates more reliably with crack severity than frequency modulation. The authors provided a clear indication of damage progression by isolating the amplitude component.

Donskoy and Ramezani [18] suggested an algorithm to separate amplitude and frequency modulation indices in VAM in 2018. Furthermore, they introduced a Non-Modulated Carrier (NMC), an HF wave part that did not pass through defects and remained non-modulated. The amplitude and phase shift of the NMC change due to wave propagation. Since the modulated signal and NMC have the same primary (carrier) frequency, which is ω, the summation of these signals contaminates the amplitude and the phase shift of the measured signal at the frequency ω. Therefore, they suggested a time-domain algorithm, the Sweeping-Phase Homodyne Separation (SPHS), to separate the amplitude and frequency modulation indices using the first sidebands (left and right) to avoid using the contaminated carrier frequency. The results published by Donskoy and Ramezani showed that the SPHS algorithm can successfully separate the amplitude and frequency modulation indices in the presence of an NMC. Their experimental results revealed that the frequency modulation index (FMI) was larger than the amplitude modulation index (AMI) at the earlier stage of the defect. Then, AMI became larger than FMI at the end of a fatigue damage evolution [18]. In another work in 2019 [19], they reported that early micro-crack stages exhibit mostly frequency modulation, while amplitude modulation becomes pronounced during macro-crack formation.

Klepka et al. [20] examined nonlinear modulation effects in vibro-acoustic tests for detecting contact-type damage using HT. They identified that modulation patterns, notably amplitude and frequency modulations, depend heavily on excitation amplitudes and interactions between low- and high-frequency signals with damaged surfaces.

In 2020, Opperman et al. [21] employed mathematical approaches to explain amplitude and phase modulation, using a short-time Fourier transform (STFT) to estimate them separately. They noted that their results could not confirm whether either AM or PM/FM is a reliable index for revealing a defect.

Gorski et al. [22] investigate the Modulation Transfer (MT) phenomenon, also known as the Luxembourg–Gorky effect, within the context of nonlinear elastic wave theory for damage localization. The authors propose a novel signal processing approach capable of separating Amplitude Modulation (AM) and Frequency Modulation (FM) components from the structural response, based on the HT. They concluded that the observed FM components likely arise from Time-of-Flight (ToF) modulation. They hypothesized that the pumping wave induces stress-dependent variations in wave propagation velocity and path length at the crack interface, which manifests as phase and, consequently, frequency modulation in the probing signal.

In summary, from the literature reviewed, the following challenges or questions regarding defect detection and modulation indices still exist:

1. Previous studies in this field have clearly confirmed the presence of at least two types of modulation in the response signal, amplitude modulation and either frequency or phase modulation [11,12,17,18,20–22]. However, the possibility of all three modulation types (amplitude, frequency, and phase) coexisting needs further investigation.
2. The MI separation techniques proposed by researchers examine the relationship between the nonlinear behavior of the structure under test (SUT) and the corresponding measured response parameters. However, the possibility of early crack detection using these parameters remains to be investigated.
3. The proposed methods for MI separation are developed based on the mathematical representation of the modulation phenomena observed in the measured response. The selected model must accurately characterize the response behavior (amplitude and phase shift) throughout its lifetime.
4. Although Hilbert transform-based methods have high potential for simultaneously analyzing the amplitude and phase of the measured response, the presence of a non-modulated carrier (NMC) can lead to inaccurate results. Therefore, techniques that provide more reliable results are required.

Despite advancements in modulation indices (MIs) separation and damage-detection techniques, the relationship between MIs and damage progression remains unclear and requires further mathematical clarification. Notably, this relationship highly depends on the chosen signal model and its parameters. In this study, we propose a comprehensive model that integrates amplitude, frequency, and phase modulation simultaneously. This model represents changes in the phase shifts of different frequency components as a function of MIs, as confirmed by experimental results.

2. Methodology

As mentioned earlier, the experimental results [11,12,17,18,20–22] confirm the presence of two distinct modulation types, amplitude and frequency/phase modulation, in the VAM-measured response. The easiest way to mathematically describe modulation is to consider a single-tone HF (carrier) signal modulated by a single-tone LF signal. The modulation model must be able to describe changes in the parameters of the measured response (amplitude and phase shift) as MIs vary.

The most commonly employed model for describing the measured signal and MI separation is a combination of amplitude and frequency modulation [17,18]. This model is referred to as AFM in subsequent references. However, this model cannot fully describe the behavior of the measured response over its lifetime, whereas MIs vary. In this research, a combination of all three modulation types (an amplitude–frequency–phase modulation) is introduced and described mathematically. This model is also referred to as AFPM in subsequent references. The following subsections represent both AFM and AFPM models and their differences.

2.1. An Amplitude–Frequency Modulation Model

In this modulation, both the amplitude and frequency of the HF signal change based on the LF signal, which is illustrated in Equation (2), where m_a and m_f quantify the amount of amplitude and frequency modulations, respectively. The number of sidebands in this model is theoretically infinite [1,10,13,23–26], which is shown in Figure 2a. Table 1 represents the amplitude and phase shift of the AFM signal components after replacing $X_\Omega(t)$, defined in Equation (1), into the Equation (2). As evident in Table 1, the phase shifts of the signal components remain unchanged despite changes in the MIs, and the amplitude of the corresponding sidebands ($|A_{\pm n}|$) are not symmetric in this model (see Figure 2b). It

is noticeable that the amplitude of the corresponding sidebands ($|A_{\pm n}|$) are symmetric in an amplitude and phase modulation model.

$$A_\omega(1 + 2m_a X_\Omega(t))cos\left(\omega t + \phi_\omega + 2m_f \int X_\Omega(t)dt\right) \quad (2)$$

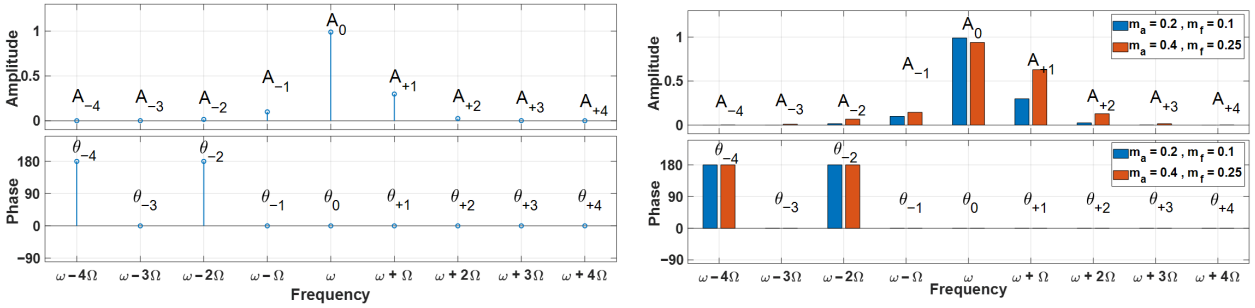

(**a**) (**b**)

Figure 2. The FFT spectrum of a simulated AFM signal using MATLAB 2024b: (**a**) the number of sidebands is theoretically infinite, and the phase shifts are 0 or π in the signals (see Table 1); (**b**) the phase shift of the signal components remains unchanged despite changes in the modulation indices (see Table 1).

Table 1. The amplitude and phase shift for different signal components in an amplitude–frequency modulated (AFM) signal when HF and LF signals are single-tone waveforms.

Frequency	Amplitude	Phase Shift
ω	$A_0 = A_\omega J_0\left(2m_f A_\Omega\right)$	$\theta_0 = \phi_\omega$
$\omega + \Omega$	$A_{+1} = A_\omega\left(J_1\left(2m_f A_\Omega\right) + m_a A_\Omega J_0\left(2m_f A_\Omega\right) + m_a A_\Omega J_2\left(2m_f A_\Omega\right)\right)$	$\theta_{+1} = \phi_\omega + \phi_\Omega$
$\omega - \Omega$	$A_{-1} = A_\omega\left(-J_1\left(2m_f A_\Omega\right) + m_a A_\Omega J_0\left(2m_f A_\Omega\right) + m_a A_\Omega J_2\left(2m_f A_\Omega\right)\right)$	$\theta_{-1} = \phi_\omega - \phi_\Omega$
$\omega + 2\Omega$	$A_{+2} = A_\omega\left(J_2\left(2m_f A_\Omega\right) + m_a A_\Omega J_1\left(2m_f A_\Omega\right) + m_a A_\Omega J_3\left(2m_f A_\Omega\right)\right)$	$\theta_{+2} = \phi_\omega + 2\phi_\Omega$
$\omega - 2\Omega$	$A_{-2} = A_\omega\left(J_2\left(2m_f A_\Omega\right) - m_a A_\Omega J_1\left(2m_f A_\Omega\right) - m_a A_\Omega J_3\left(2m_f A_\Omega\right)\right)$	$\theta_{-2} = \phi_\omega - 2\phi_\Omega$
$\omega + n\Omega$	$A_{+n} = A_\omega\left(J_n\left(2m_f A_\Omega\right) + m_a A_\Omega J_{n-1}\left(2m_f A_\Omega\right) + m_a A_\Omega J_{n+1}\left(2m_f A_\Omega\right)\right)$	$\theta_{+n} = \phi_\omega + n\phi_\Omega$
$\omega - n\Omega$	$A_{+n} = (-1)^n A_\omega\left(J_n\left(2m_f A_\Omega\right) - m_a A_\Omega J_{n-1}\left(2m_f A_\Omega\right) - m_a A_\Omega J_{n+1}\left(2m_f A_\Omega\right)\right)$	$\theta_{-n} = \phi_\omega - n\phi_\Omega$

2.2. An Amplitude–Frequency–Phase Modulation Model

The mathematical description of this model is not presented in reference books and is presented here for the first time. In this model, the amplitude, frequency, and phase of the HF signal change based on the LF signal, which is illustrated in Equation (3), where m_a, m_f, and m_p, quantifies amplitude, frequency, and phase modulations. This model can be converted to an Amplitude–Phase modulated signal with a new modulation index by using some trigonometric identities illustrated in Equation (4). The number of sidebands in this model is also theoretically infinite, as shown in Figure 3a. Tables 2 and 3 represent the amplitude and phase shift of the AFPM signal components after replacing $X_\Omega(t)$, defined in Equation (1), into Equation (3). As evident in Tables 2 and 3, the phase shifts and the amplitude of the signal components vary with the change in the modulation indices (see Figure 3b,d), and the amplitude of the corresponding sidebands ($|A_{\pm n}|$) are not symmetric in this model.

$$A_\omega(1 + 2m_a X_\Omega(t))cos\left(2\pi f_\omega t + \phi_\omega + 2m_p\, X_\Omega(t) + 2m_f \int X_\Omega(t)dt\right) \quad (3)$$

$$A_\omega(1+2m_aA_\Omega cos(\Omega t+\phi_\Omega))cos\Big(\omega t+\phi_\omega+2m_p\ A_\Omega cos(\Omega t+\phi_\Omega)+2m_f\ A_\Omega sin(\Omega t+\phi_\Omega)\Big)$$

$$A_\omega(1+2m_aA_\Omega cos(\Omega t+\phi_\Omega))cos\left(\omega t+\phi_\omega+2A_\Omega\sqrt{{m_f}^2+{m_p}^2}\ cos\left(\Omega t+\phi_\Omega-tan^{-1}\left(\frac{m_f}{m_p}\right)\right)\right) \quad (4)$$

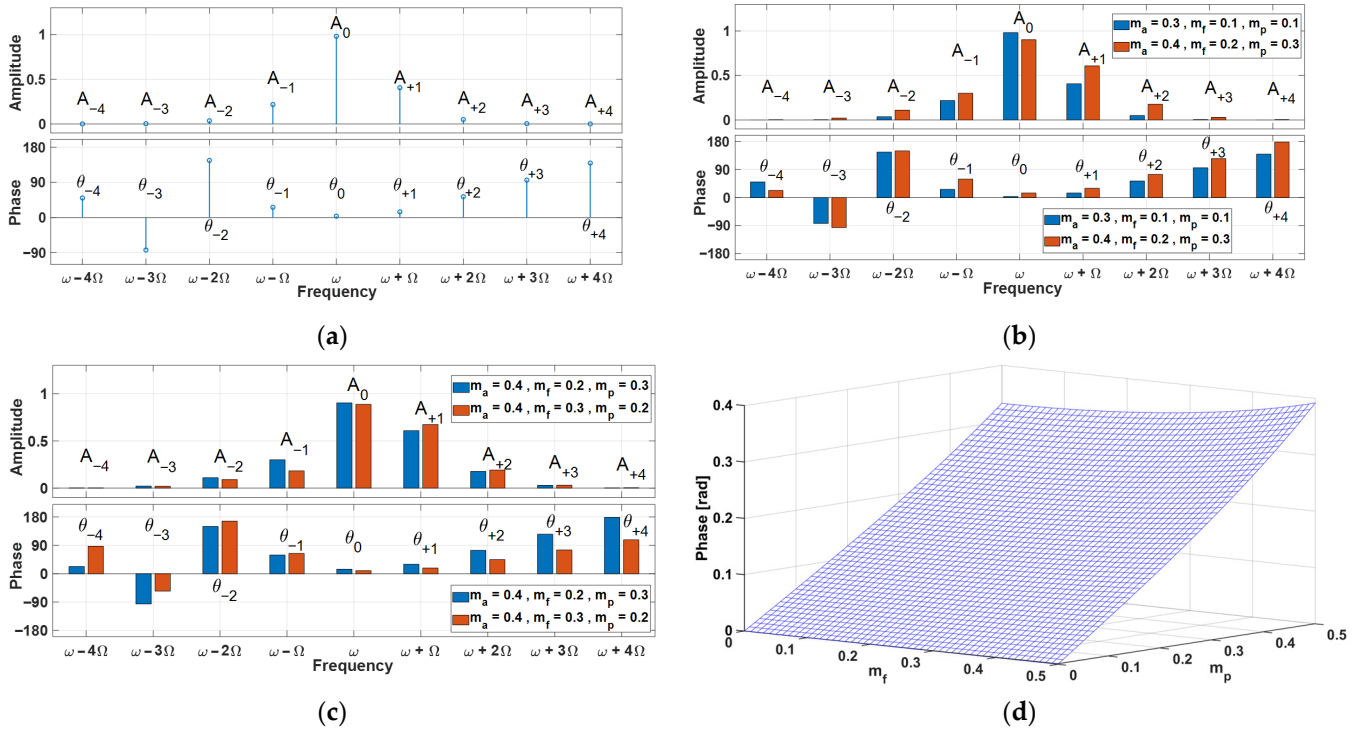

Figure 3. The FFT spectrum of a simulated AFPM signal using MATLAB: (**a**) the number of sidebands is theoretically infinite, and the phase shift of the signal components changes based on Table 3; (**b**) phase shifts of the signal components vary with the change in the MIs (see Table 3); (**c**) amplitudes and phase shifts are different when $m_{a_2} = m_{a_1}$, $m_{f_2} = m_{p_1}$ and $m_{p_2} = m_{f_1}$; (**d**) a 3D plot of the phase shift of the primary frequency component, θ_0, when $m_a = 0.3$ and m_f and m_p vary from 0 to 0.5 (see Table 3).

Table 2. The amplitude of different signal components in an AFPM signal when HF and LF signals are single-tone waveforms, where $z = 2A_\Omega\sqrt{{m_f}^2+{m_p}^2}$ and $\beta = tan^{-1}\left(\frac{m_f}{m_p}\right)$.

Frequency	Amplitude	
ω	$A_0 = A_\omega\sqrt{(a_0)^2+(b_0)^2}$	$a_0 = J_0(z)$ $b_0 = -2m_aA_\Omega J_1(z)cos(\beta)$
$\omega+\Omega$	$A_{+1} = A_\omega\sqrt{(a_{+1})^2+(b_{+1})^2}$	$a_{+1} = m_aA_\Omega J_0(z) - m_aA_\Omega J_2(z)cos(2\beta) + J_1(z)sin(\beta)$ $b_{+1} = -m_aA_\Omega J_2(z)sin(2\beta) - J_1(z)cos(\beta)$
$\omega-\Omega$	$A_{-1} = A_\omega\sqrt{(a_{+1})^2+(b_{+1})^2}$	$a_{-1} = m_aA_\Omega J_0(z) - m_aA_\Omega J_2(z)cos(2\beta) - J_1(z)sin(\beta)$ $b_{-1} = m_aA_\Omega J_2(z)sin(2\beta) - J_1(z)cos(\beta)$
$\omega+2\Omega$	$A_{+2} = A_\omega\sqrt{(a_{+1})^2+(b_{+1})^2}$	$a_{+2} = -J_2(z)cos(2\beta) + m_aA_\Omega J_1(z)sin(\beta) - m_aA_\Omega J_3(z)sin(3\beta)$ $b_{+2} = -J_2(z)sin(2\beta) - m_aA_\Omega J_1(z)cos(\beta) + m_aA_\Omega J_3(z)cos(3\beta)$
$\omega-2\Omega$	$A_{-2} = A_\omega\sqrt{(a_{+1})^2+(b_{+1})^2}$	$a_{-2} = -J_2(z)cos(2\beta) - m_aA_\Omega J_1(z)sin(\beta) + m_aA_\Omega J_3(z)sin(3\beta)$ $b_{-2} = J_2(z)sin(2\beta) - m_aA_\Omega J_1(z)cos(\beta) + m_aA_\Omega J_3(z)cos(3\beta)$

Table 3. The phase shift of different signal components in an AFPM signal.

Frequency	Phase Shift	
ω	$\theta_0 = \phi_\omega - tan^{-1}\left(\frac{b_0}{a_0}\right)$	$a_0 = J_0(z)$ $b_0 = -2m_a A_\Omega J_1(z)cos(\beta)$
$\omega + \Omega$	$\theta_{+1} = \phi_\omega + \phi_\Omega - tan^{-1}\left(\frac{b_{+1}}{a_{+1}}\right)$	$a_{+1} = m_a A_\Omega J_0(z) - m_a A_\Omega J_2(z)cos(2\beta) + J_1(z)sin(\beta)$ $b_{+1} = -m_a A_\Omega J_2(z)sin(2\beta) - J_1(z)cos(\beta)$
$\omega - \Omega$	$\theta_{-1} = \phi_\omega - \phi_\Omega - tan^{-1}\left(\frac{b_{-1}}{a_{-1}}\right)$	$a_{-1} = m_a A_\Omega J_0(z) - m_a A_\Omega J_2(z)cos(2\beta) - J_1(z)sin(\beta)$ $b_{-1} = m_a A_\Omega J_2(z)sin(2\beta) - J_1(z)cos(\beta)$
$\omega + 2\Omega$	$\theta_{+2} = \phi_\omega + 2\phi_\Omega - tan^{-1}\left(\frac{b_{+2}}{a_{+2}}\right)$	$a_{+2} = -J_2(z)cos(2\beta) + m_a A_\Omega J_1(z)sin(\beta) - m_a A_\Omega J_3(z)sin(3\beta)$ $b_{+2} = -J_2(z)sin(2\beta) - m_a A_\Omega J_1(z)cos(\beta) + m_a A_\Omega J_3(z)cos(3\beta)$
$\omega - 2\Omega$	$\theta_{-2} = \phi_\omega - 2\phi_\Omega - tan^{-1}\left(\frac{b_{-2}}{a_{-2}}\right)$	$a_{-2} = -J_2(z)cos(2\beta) - m_a A_\Omega J_1(z)sin(\beta) + m_a A_\Omega J_3(z)sin(3\beta)$ $b_{-2} = J_2(z)sin(2\beta) - m_a A_\Omega J_1(z)cos(\beta) + m_a A_\Omega J_3(z)cos(3\beta)$

2.3. The Phase Shifts Are the Distinguishing Feature

The amplitude of the frequency spectrum of the measured response is insufficient for determining the appropriate modulation model. As shown in Figures 2a and 3a, both AFM and AFPM have the same features: (1) infinite sidebands and (2) non-symmetrical sideband amplitudes. Therefore, the phase of the frequency spectrum of the measured response must also be considered in this decision.

As shown in Table 3, all signal components in the AFPM model exhibit an additional phase shift related to the MIs. However, the phase shift of all components for the AFM model remains constant with changes in m_a or m_f. Figure 4 shows an example of 3D plots of the phase shift of a MATLAB-simulated signal at the primary frequency, ϕ_ω, for both AFM and AFPM models (see Tables 1 and 3).

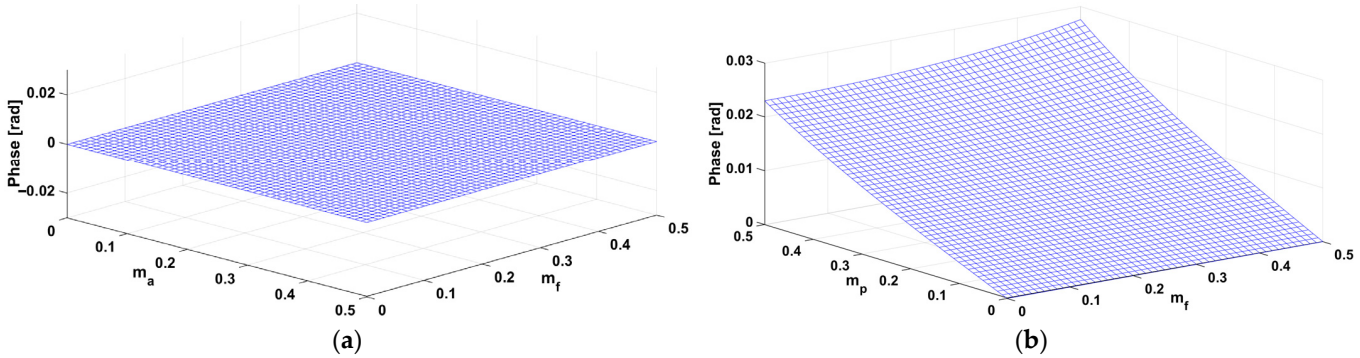

Figure 4. The 3D plot of the phase shift at frequency ω, where the initial phase shifts are set to ϕ_ω, $\phi_\Omega = 0$; (**a**) an AFM simulated signal; (**b**) an AFPM simulated signal for a constant $m_a = 0.02$.

Experimental results [10,17–20] confirmed that MIs evolve over the lifetime of the SUT. Consequently, variations in the phase shift of different frequency components within the measured response provide clear evidence supporting the possible coexistence of all three modulation types.

2.4. Relative Sensitivity of the DMI and Phase Shifts

Researchers have suggested different parameters to quantify the effect of a defect on the system response. The most popular parameter quantifying modulation is the Damage Modulation Index (DMI), defined by Donskoy [1] and given in Equation (5), where $A_{\pm1,0}$ represent the amplitude of sidebands and the primary frequency defined before [1,10,27,28]. This parameter was initially called Modulation Index (MI) by Donskoy, but will be called the Damage Modulation Index (DMI), to avoid overlapping with the signal modulation index.

$$DMI = \frac{A_{+1} + A_{-1}}{2A_0} \tag{5}$$

The sensitivity of phase shifts and DMI to changes in modulation index can be investigated by examining the relative sensitivities of both functions. The relative sensitivity (RS) of a function to its variable is given in Equation (6).

$$Relative\ Sensitivity\ of\ F(x_1, x_2, x_3, \ldots, x_n)\ to\ x_k\ \equiv S^F_{x_k} = \frac{\partial F}{\partial x_k}\ \frac{x_k}{F} \tag{6}$$

Equations (7) and (8) represent the relationship between DMI and the summation of phase shifts of the first sidebands See Section 3.3, Φ, as functions of MIs for an AFPM model, where A_{+1}, A_{-1}, A_0, θ_{+1}, θ_{-1}, β and z are represented in Tables 2 and 3.

$$DMI\left(m_a, m_f, m_p\right) = \frac{A_{+1} + A_{-1}}{2A_0}$$

$$DMI = \frac{\sqrt{(m_a A_\Omega)^2 (J_0 - J_2)^2 \cos^2\beta + (m_a A_\Omega (J_0 + J_2)\sin\beta + J_1)^2} + \sqrt{(m_a A_\Omega)^2 (J_0 - J_2)^2 \cos^2\beta + (m_a A_\Omega (J_0 + J_2)\sin\beta - J_1)^2}}{2\sqrt{J_0^2 + 4\,(m_a A_\Omega)^2\, J_1^2 \cos^2\beta}} \tag{7}$$

$$\Phi\left(m_a, m_f, m_p\right) = \theta_{+1} + \theta_{-1}$$

$$\Phi = -tan^{-1}\left(\frac{b_{+1}}{a_{+1}}\right) - tan^{-1}\left(\frac{b_{-1}}{a_{-1}}\right)$$

$$\Phi = -tan^{-1}\left(\frac{-m_a A_\Omega J_2(z) sin(2\beta) - J_1(z) cos(\beta)}{m_a A_\Omega J_0(z) - m_a A_\Omega J_2(z) cos(2\beta) + J_1(z) sin(\beta)}\right) - tan^{-1}\left(\frac{m_a A_\Omega J_2(z) sin(2\beta) - J_1(z) cos(\beta)}{m_a A_\Omega J_0(z) - m_a A_\Omega J_2(z) cos(2\beta) - J_1(z) sin(\beta)}\right) \tag{8}$$

The RS of both DMI and Φ for each MI can be calculated using Equation (6). Finally, the second norm ($\|f\|_2 = \sqrt{\sum |f_i|^2}$, *where* $f = [f_1, f_2, f_3, \ldots, f_n]$) for each MI is calculated as the RS of DMI and Φ, as given in Equations (9) and (10).

$$Relative\ Sensitivity\ of\ DMI = \sqrt{\left(\frac{\partial DMI}{\partial m_a}\ \frac{m_a}{DMI}\right)^2 + \left(\frac{\partial DMI}{\partial m_f}\ \frac{m_f}{DMI}\right)^2 + \left(\frac{\partial DMI}{\partial m_p}\ \frac{m_p}{DMI}\right)^2} \tag{9}$$

$$Relative\ Sensitivity\ of\ \Phi = \sqrt{\left(\frac{\partial \Phi}{\partial m_a}\ \frac{m_a}{\Phi}\right)^2 + \left(\frac{\partial \Phi}{\partial m_f}\ \frac{m_f}{\Phi}\right)^2 + \left(\frac{\partial \Phi}{\partial m_p}\ \frac{m_p}{\Phi}\right)^2} \tag{10}$$

MATLAB 2024b was used to numerically evaluate and compare the relative sensitivities of the DMI and Φ with respect to variations in the variables. Since RS depends on three variables m_a, m_f and m_p, a complete visualization would be four-dimensional. To simplify plotting, the parameter m_a is held fixed, and a three-dimensional surface is rendered over $\left(m_f, m_p\right)$. At each simulation step, a value is assigned to m_a and the RS is computed. This procedure is then repeated for multiple m_a values. The ranges and magnitudes of the variable changes are represented in Table 4.

Figure 5 illustrates the 3D plot of the RS for both $DMI\left(m_a, m_f, m_p\right)$ and $\Phi\left(m_a, m_f, m_p\right)$ in three different values of m_a. As it is evident, the RS value of $\Phi\left(m_a, m_f, m_p\right)$ is bigger than $DMI\left(m_a, m_f, m_p\right)$, which means that the $\Phi\left(m_a, m_f, m_p\right)$ is more sensitive than $DMI\left(m_a, m_f, m_p\right)$ when any of the MIs change.

Table 4. The details of the variables used in the relative sensitivity calculation using MATLAB.

Variable	Min	Step	Max
m_a	1×10^{-6}	1×10^{-5}	1×10^{-3}
m_p	1×10^{-6}	1×10^{-5}	1×10^{-3}
m_f	1×10^{-6}	1×10^{-5}	1×10^{-3}

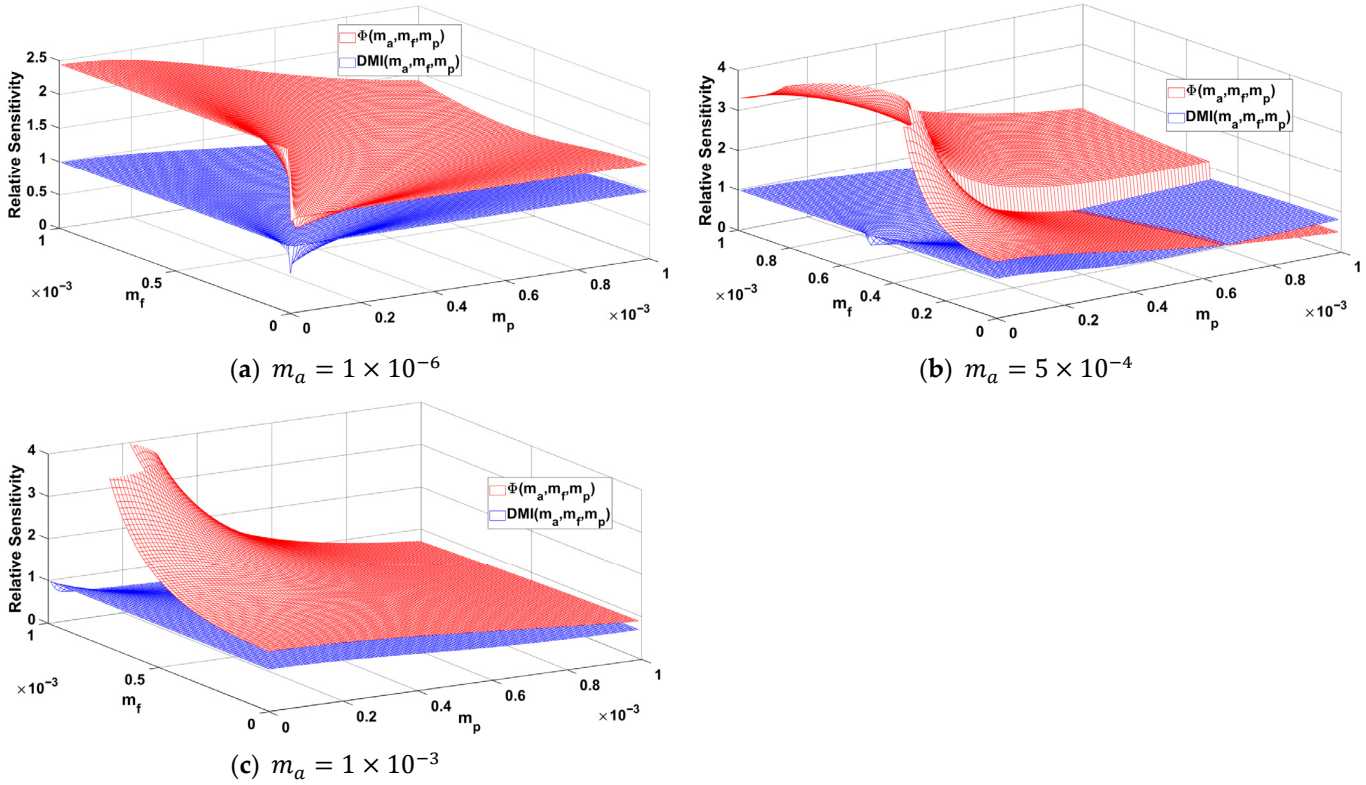

(**a**) $m_a = 1 \times 10^{-6}$ (**b**) $m_a = 5 \times 10^{-4}$

(**c**) $m_a = 1 \times 10^{-3}$

Figure 5. The 3D plot of the relative sensitivity (RS) of $DMI\left(m_a, m_f, m_p\right)$ and $\Phi\left(m_a, m_f, m_p\right)$ evaluated in MATLAB 2024b, when (**a**) $m_a = 1 \times 10^{-6}$, (**b**) $m_a = 5 \times 10^{-4}$, and (**c**) $m_a = 1 \times 10^{-3}$.

The higher sensitivity of $\Phi\left(m_a, m_f, m_p\right)$ compared with $DMI\left(m_a, m_f, m_p\right)$ implies that variations in the MIs induce larger changes in $\Phi\left(m_a, m_f, m_p\right)$, which can be exploited for early defect detection. However, it should be emphasized that at the early stage of crack initiation, the variation in phase shift or amplitude of different frequency components is insignificant and may be masked by noise or measurement errors. Utilizing high-precision instrumentation in conjunction with robust noise-reduction techniques can enhance the reliability of the results.

3. Experimental Results

To experimentally validate the applicability of the AFPM model, this section investigates whether the model can capture phase-shift variations in the VAM response induced by changes in MIs. Unlike the AFM model, the AFPM model predicts that the phase shifts of frequency components vary with the MIs. Table 5 provides a direct comparison of the theoretical phase shifts predicted by both models. The following experimental procedure is designed to isolate and evaluate these shifts, thereby confirming the presence of phase-modulation.

3.1. Test Setup

The variation in phase shift of the VAM response is experimentally investigated using aluminum specimens with a thickness of 3 mm, as shown in Figure 6. Two piezoceramics

(PI255) with a diameter of 10 mm are attached to one side of the sample to excite the HF signal and measure the system response simultaneously.

Table 5. The phase shifts at different frequency components in the AFM and AFPM models.

Frequency	Phase Shifts in the	
	AFM Model	**AFPM Model**
ω	ϕ_ω	$\theta_0 = \phi_\omega - tan^{-1}\left(\frac{-2m_a A_\Omega J_1(z)cos(\beta)}{J_0(z)}\right)$
		$\theta_0 = \phi_\omega + \theta_{MP0}$
$\omega + \Omega$	$\phi_\omega + \phi_\Omega$	$\theta_{+1} = \phi_\omega + \phi_\Omega - tan^{-1}\left(\frac{-m_a A_\Omega J_2(z)sin(2\beta) - J_1(z)cos(\beta)}{m_a A_\Omega J_0(z) - m_a A_\Omega J_2(z)cos(2\beta) + J_1(z)sin(\beta)}\right)$
		$\theta_{+1} = \phi_\omega + \phi_\Omega + \theta_{MP+1}$
$\omega - \Omega$	$\phi_\omega - \phi_\Omega$	$\theta_{-1} = \phi_\omega - \phi_\Omega - tan^{-1}\left(\frac{m_a A_\Omega J_2(z)sin(2\beta) - J_1(z)cos(\beta)}{m_a A_\Omega J_0(z) - m_a A_\Omega J_2(z)cos(2\beta) - J_1(z)sin(\beta)}\right)$
		$\theta_{-1} = \phi_\omega - \phi_\Omega + \theta_{MP-1}$

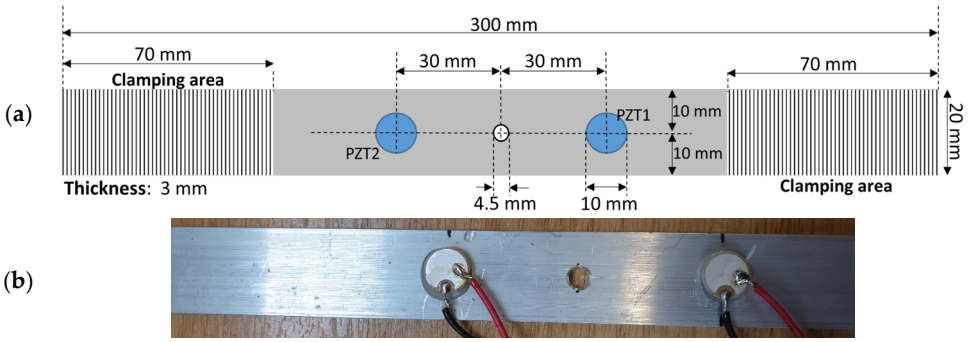

Figure 6. A general setup for the MI separation algorithm; (**a**) schematic sketch of the test setup; (**b**) an experimental setup.

The LF signal is applied using a tensile hydraulic machine, INSTRON 250 kN, at a frequency of $f_\Omega = 10$ Hz and the amplitude of 1.5 kN (0–1.5 kN), as shown in Figure 7a. After measuring the VAM response for all selected frequencies, the amplitude of the LF is changed to 10 kN (0–10 kN) to induce fatigue in the SUT for a certain number of cycles, as shown in Figure 7b. The procedure repeats until the sample breaks. A National Instruments Multifunction I/O device, USB-6366, is used to send the signal into the actuator and measure the system response simultaneously, and a MATLAB script controls the process.

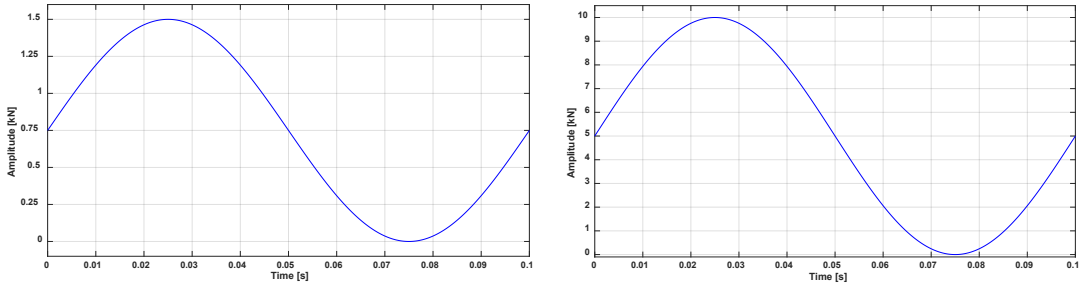

Figure 7. The LF load amplitude: (**a**) during the VAM measurement; (**b**) fatigue load.

3.2. High Frequency Selection

A single-tone HF signal at a specific frequency is generated in MATLAB and applied to the actuator on the sample using an NI device. The signal at the receiver is measured

simultaneously. The amplitude of the measured signal, calculated by the FFT, is saved in a matrix. The process of sending and measuring the HF signal is repeated over a specific range of frequencies. A sample of the linear sweep result is shown in Figure 8a,b. A frequency or range of frequencies with high amplitudes is selected at the receiver for the VAM measurement process. The frequency selection can also be achieved using chirp excitation, as illustrated in Figure 8c. As shown in Figure 8d, an eigenfrequency of the sample can also be detected using single-tone excitation (known as a linear sweep method).

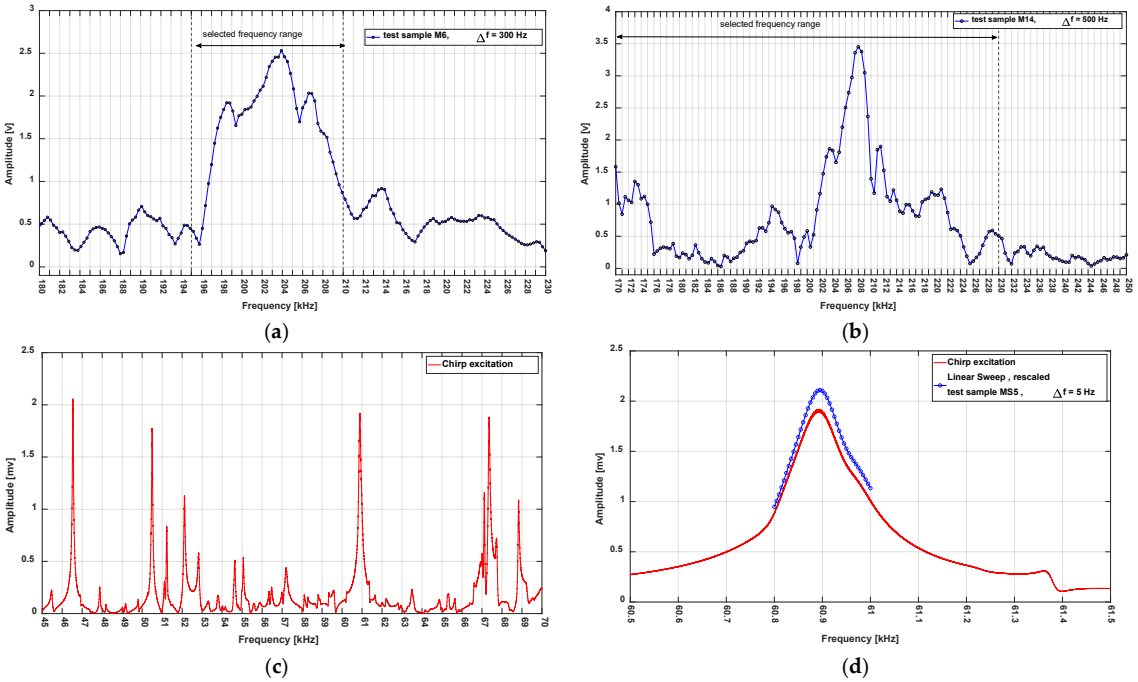

Figure 8. Frequency selection using the linear sweep; (**a**) linear sweep result for a test sample M6; (**b**) linear sweep result for a test sample M14; (**c**) FFT result of a chirp excitation for test sample MS5; (**d**) comparison between the chirp and single-tone excitation method results around an eigenfrequency at [60.8–60.9] kHz for the test sample MS5.

3.3. Angle Modulation Phase Shift

To investigate the phase shift of the VAM response, a test setup, represented in Figure 9, is prepared to measure the VAM response of a sample and the sent HF signal simultaneously. The phase shifts that are written in the figure are introduced in the following:

- θ_ω represents the HF signal phase shift. The value of the θ_ω is arbitrary.
- θ_Ω represents the LF signal phase shift. The value of the θ_Ω is arbitrary.
- θ_{pz1-2} represents the change in signal phase shift due to a piezoelectric.
- θ_{sp} represents the signal phase shift introduced by the sample, such as propagation delay.
- θ_{MP} represents the change in signal phase shift due to the modulation itself (see Table 3).

The phase shift of the first sideband was selected for investigation in this test setup to avoid contamination of the measured response by the non-modulated carrier (NMC) component. The value of θ_ω, θ_{pz1-2} and θ_{sp} are arbitrary and θ_{MP} is the phase shift that is being calculated. Since the sent signal and response were measured simultaneously, the value of θ_ω can be set to 0 by comparing the sent and measured responses, as represented in Figure 10, or can be eliminated by subtracting the sent signal phase shift calculated by FFT from the measured response phase shift at the end of the phase calculation. Thus, the value of θ_ω is assumed to be 0 for subsequent calculations to simplify.

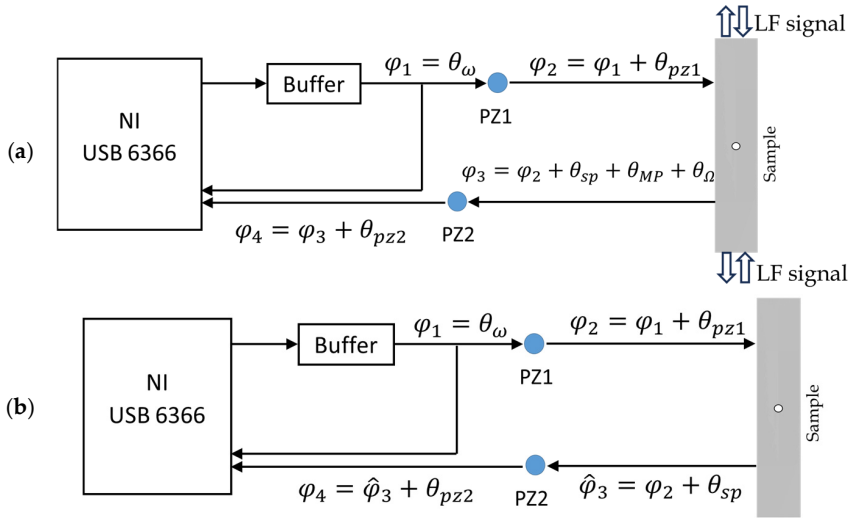

Figure 9. The test setup for phase shifts measurement: (**a**) the VAM response setup; (**b**) the HF response setup.

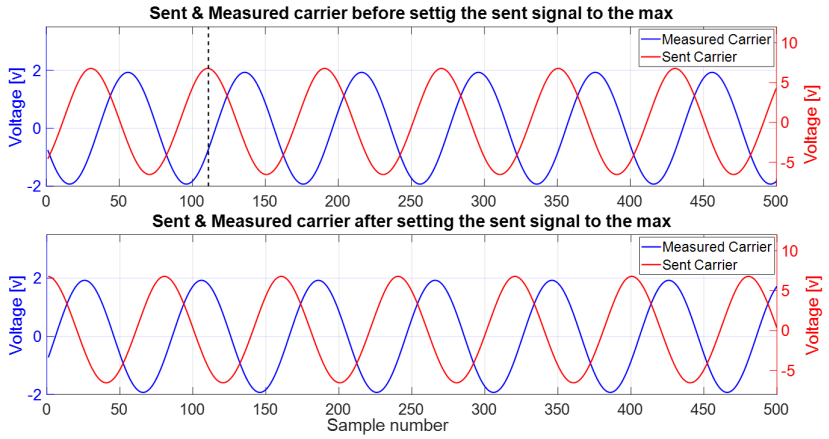

Figure 10. The value of θ_ω can be set to 0 by comparing the sent and measured response.

The phase shift of the VAM response signal at $\omega \pm \Omega$ using the phase shifts listed in Figure 8a is given in Equation (11). Using the $\theta_{+1} + \theta_{-1}$ helps us to delete the value θ_Ω of the equations, especially considering that the value of θ_Ω is unidentified, as represented in Equation (12).

$$\begin{aligned} \theta_{+1} &= \theta_\omega + \theta_\Omega + \theta_{pz1} + \theta_{pz2} + \theta_{sp_{+1}} + \theta_{MP+1} \quad \text{(a)} \\ \theta_{-1} &= \theta_\omega - \theta_\Omega + \theta_{pz1} + \theta_{pz2} + \theta_{sp_{-1}} + \theta_{MP-1} \quad \text{(b)} \end{aligned} \tag{11}$$

$$\theta_{+1} + \theta_{-1} = \left(\theta_\omega + \theta_{pz1} + \theta_{pz2} + \theta_{sp_{+1}}\right) + \left(\theta_\omega + \theta_{pz1} + \theta_{pz2} + \theta_{sp_{-1}}\right) + \left(\theta_{MP+1} + \theta_{MP-1}\right) \tag{12}$$

The phase shift of the HF response signal at ω using the phase shifts listed in Figure 8b is given in Equation (13). By comparing the last two equations, it is evident that the terms present in Equation (12) are essentially the same as the signal phase shift in Equation (13), but correspond to different frequencies.

To compare the phase shift of an HF signal at sideband frequencies, a single-tone sinusoidal waveform at different frequencies was applied to a test sample, and the phase shift was calculated using the measured response at the receiver, as represented in Figure 8a. Figure 11 shows the measured HF response phase shifts at different frequencies. The frequency of the HF signal was selected equal to $\omega \pm k\Omega$ for $k = 0, 1, 2, \cdots$ to compare the phase shift at different sidebands' frequencies.

$$\varphi_{4_\omega} = \theta_\omega + \theta_{pz1} + \theta_{pz2} + \theta_{sp} \tag{13}$$

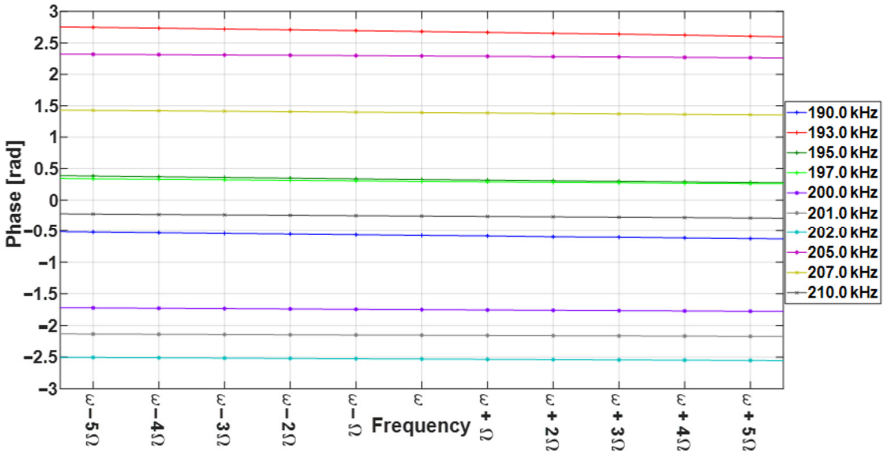

Figure 11. The HF response phase shift (φ_4) at different frequencies, $\omega \pm (k \times 10)$ Hz for $k = 0, 1, 2, \cdots$.

Results reveal that the phase shifts (φ_{4_ω}) at $\omega \pm \Omega$ and ω are almost equal, and the difference between phase shifts are negligible. Considering this finding, Equation (12) can be written as Equation (14). Finally, the value of the $\theta_{MP+1} + \theta_{MP-1}$, which is called angle modulation phase shift (θ_{AngM}), can be calculated using Equation (15). Figure 11 illustrates the results of the θ_{AngM} calculated at different frequencies.

$$\theta_{+1} + \theta_{-1} = (\varphi_{4_\omega}) + (\varphi_{4_\omega}) + (\theta_{MP+1} + \theta_{MP-1}) \tag{14}$$

$$\Phi\Big(m_a, m_f, m_p\Big) \equiv \theta_{AngM} = (\theta_{MP+1} + \theta_{MP-1}) = (\theta_{+1} + \theta_{-1}) - 2\varphi_{4_\omega} \tag{15}$$

As evident in Figure 12, θ_{AngM} changes through the life cycle and reveals that phase shift changes with MIs. As noted earlier, the AFM model fails to explain the phase-shift variations associated with changes in MI. In contrast, the AFPM model successfully predicts these variations, which are also evident in experimental observations.

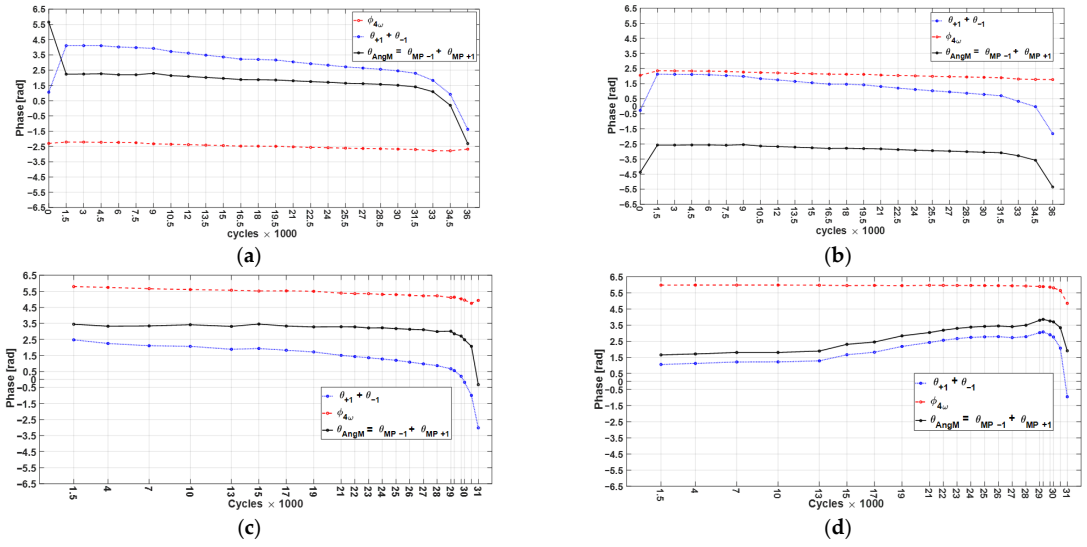

Figure 12. Results of the calculated θ_{AngM} using Equation (15); (**a**) M6 test series, $\omega = 201.0$ kHz; (**b**) M6 test series, $\omega = 206.0$ kHz; (**c**) M14 test series, $\omega = 175.0$ kHz; (**d**) M14 test series, $\omega = 197.0$ kHz.

Figure 13 demonstrates that the angle-modulation phase shift, θ_{AngM}, evolves consistently as the crack grows, confirming that phase information is fundamentally linked to the MIs, as predicted by the AFPM model. The measured θ_{AngM} provides direct experimental evidence that phase (PM) and frequency (FM) contributions coexist with amplitude modulation in the VAM response.

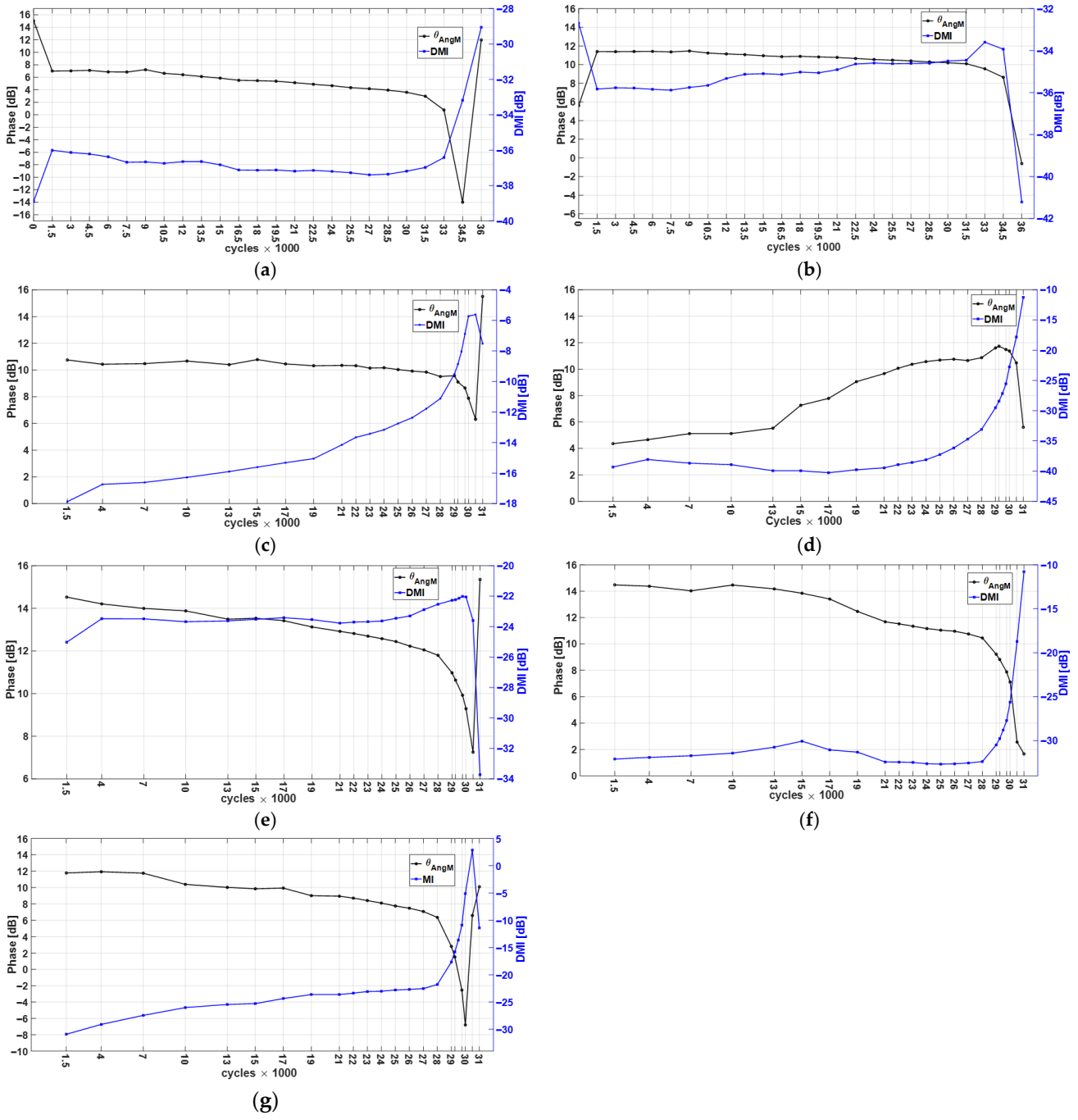

Figure 13. Comparison between the MI and θ_{AngM}; (**a**) M6 test series, $\omega = 201.0$ kHz; (**b**) M6 test series, $\omega = 206.0$ kHz; (**c**) M14 test series, $\omega = 175.0$ kHz; (**d**) M14 test series, $\omega = 197.0$ kHz; (**e**) M14 test series, $\omega = 194.0$ kHz; (**f**) M14 test series, $\omega = 230.0$ kHz; (**g**) M14 test series, $\omega = 231.0$ kHz.

4. Discussion

The angle-modulation phase shift, θ_{AngM}, and damage modulation index (DMI) curves obtained from the experimental results are analyzed to assess their potential for early defect detection.

Since specimens M6 and M14 failed after around 36,500 and 31,200 cycles, respectively, the relative lifetime of each specimen, expressed as a percentage of the total number of cycles at which measurements were performed, is shown in Table 6.

Table 6. The details of the measured cycles for the M6 and M14 test setups.

M06	Cycle	0	1500	3000	4500	6000	7500	9000	10,500	12,000	13,500	15,000	16,500	18,000
	%	0	4%	8%	12%	16%	21%	25%	29%	33%	37%	41%	45%	49%
	Cycle	19,500	21,000	22,500	24,000	25,500	27,000	28,500	30,000	31,500	33,000	34,500	36,000	
	%	53%	58%	62%	66%	70%	74%	78%	82%	86%	90%	95%	99%	
M14	Cycle	1500	4000	7000	10,000	13,000	15,000	17,000	19,000	21,000	22,000	23,000	24,000	25,000
	%	5%	13%	22%	32%	42%	48%	54%	61%	67%	70%	74%	77%	80%
	Cycle	26,000	27,000	28,000	29,000	29,250	29,750	30,000	30,500	31,000				
	%	83%	86%	90%	93%	94%	95%	96%	98%	99%				

A direct comparison between the two curves is not feasible because their ranges of variation are not consistent. To eliminate this dimensional inconsistency and enable meaningful comparison, the data of both curves are normalized using Equation (16). Under the assumption that data (θ_{AngM}, DMI) at each frequency are independent of those at other frequencies, the minimum and maximum values for each frequency are used to normalize the data at that frequency.

$$x_{Norm} = \frac{x - min(x)}{max(x) - min(x)} \quad (16)$$

After data normalization, the rate of change (slope) between successive points was calculated using three different approaches:

1. Direct method: based on the normalized data.
2. Mean–mean method: slope between the mean of several consecutive points and the mean of the preceding points.
3. Point–mean method: slope between each point and the mean of its preceding points.

The slope variations of θ_{AngM} and DMI curves were compared across different frequencies and across all three calculation approaches for both the M6 and M14 test setups, as illustrated in Table 7. It should be noted that the total number of high frequencies measured at M6 and M14 test setups was 31 and 91, respectively.

Table 7. The number of frequencies in M6 and M14 where the slope of variation in θ_{AngM} is bigger than DMI.

	Type of Evaluation	**Lifetime**	**60% to 70%**	**70% to 80%**	**80% to 90%**	**60% to 75%**	**75% to 90%**	**60% to 80%**	**80% to 95%**
M6	First method	N	7	9	6	5	3	5	4
		%	22.58%	29.03%	19.35%	16.13%	9.68%	16.13%	12.9%
	Second method	N	16	13	8	15	4	13	2
		%	51.61%	41.94%	25.81%	48.39%	12.9%	41.94%	6.45%
	Third method	N	28	28	24	28	24	28	15
		%	90.32%	90.32%	77.42%	90.32%	77.42%	90.32%	48.39%
M14	First method	N	21	22	20	18	16	12	10
		%	23.08%	24.18%	21.98%	19.78%	17.58%	13.19%	10.99%
	Second method	N	19	21	25	14	19	11	18
		%	20.88%	23.08%	27.47%	15.38%	20.88%	12.09%	19.78%
	Third method	N	40	47	37	40	34	38	26
		%	43.96%	51.65%	40.66%	43.96%	37.36%	41.76%	28.57%

The following conclusions can be drawn based on the results presented in Table 7:

- The above results clearly demonstrate that, at specific frequencies, the θ_{AngM} curve is capable of revealing larger variations than the MDI curve at earlier stages.
- It is worth noting that, as with the DMI curve, which at specific frequencies does not adequately reveal the nonlinearity of the specimen, the phase curve may also fail to reflect variations in response parameters, despite its theoretical higher sensitivity.
- These results should not be interpreted as evidence of the overall superiority of phase over the DMI. As illustrated in Figure 12 and summarized in Table 7, the DMI curve exhibits greater variations at specific frequencies. Nevertheless, the findings demonstrate that incorporating phase variation analysis can enhance the sensitivity to structural changes, often revealing variations more prominently than the amplitude-based approach.

5. Conclusions

After providing a literature review of current research on modulation index (MI) separation techniques, this article introduces an experimental study on damage detection in aluminum specimens using vibro-acoustic modulation (VAM). This study introduced a modulated response model combining all three types of modulation (amplitude, frequency, and phase), called the AFPM model. Unlike the amplitude–frequency modulation (AFM) model, the mathematical description of the AFPM reveals that phase shifts across frequency components are determined not only by the initial phase shifts of the low- and high-frequency signals, but also by changes in MIs. Additionally, relative sensitivity analysis of the damage modulation index (DMI) and angle modulation phase shift (θ_{AngM}) shows that θ_{AngM} is more sensitive than DMI and can be used for detecting defects at early stages.

The change in θ_{AngM} during a lifetime is tested experimentally, and evaluating the θ_{AngM} is explained step by step. Experimental results revealed that the θ_{AngM} vary over the lifetime of the samples, as predicted by the model. Additionally, the slope between successive points, calculated by normalized values of θ_{AngM} and DMI illustrated at specific frequencies, θ_{AngM} shows more change than MI in the early stages. The results demonstrate that combining phase and amplitude variation analysis can enhance sensitivity to structural changes, often revealing them more prominently than the amplitude-based approach alone, such as the DMI.

Nevertheless, selecting a parameter or set of parameters capable of accurately indicating the onset of crack initiation in the SUT requires comprehensive experimental investigations. Such studies should combine multiple defect-detection techniques and, in parallel, employ available technologies to assess the presence or absence of cracks at different scales (macro- or micro-levels). In addition, the results in Table 7 clearly show that the frequency selection (high and low) of the excitation signals plays a crucial role in the resulting performance. Optimally selecting a frequency when the crack location is unknown requires further investigation.

Author Contributions: Conceptualization, M.M.B., N.H. and M.R.; methodology, M.M.B.; software, M.M.B.; validation, M.M.B. and M.R.; formal analysis, M.M.B.; investigation, M.M.B.; resources, M.R.; data curation, M.M.B.; writing—original draft preparation, M.M.B.; writing—review and editing, M.R. and N.H.; supervision, M.R.; project administration, M.M.B.; funding acquisition, M.R. All authors have read and agreed to the published version of the manuscript.

Funding: This research received no external funding.

Institutional Review Board Statement: Not applicable.

Informed Consent Statement: Informed consent was obtained from all subjects involved in the study.

Data Availability Statement: The raw data supporting the conclusions of this article will be made available by the authors on request.

Conflicts of Interest: The authors declare no conflicts of interest.

References

1. Donskoy, D.M.; Sutin, A.M. Vibro-Acoustic Modulation Nondestructive Evaluation Technique. *J. Intell. Mater. Syst. Struct.* **1998**, *9*, 765–771. [CrossRef]
2. Sutin, A.; Donskoy, D. Vibro-acoustic modulation nondestructive evaluation technique. In Proceedings of the Non-Destructive Evaluation Techniques for Aging Infrastructure and Manufacturing, San Antonio, TX, USA, 31 March–2 April 1998; SPIE: Bellingham, WA, USA, 1998; Volume 3397. [CrossRef]
3. Li, Z.; Wang, Z.; Xiao, L.; Qu, W. Damage detection and locating using tone burst and continuous excitation modulation method. In Proceedings of the SPIE Smart Structures and Materials + Nondestructive Evaluation and Health Monitoring, San Diego, CA, USA, 9–13 March 2014; SPIE: Bellingham, WA, USA, 2014; Volume 9064. [CrossRef]
4. Pieczonka, L.; Zietek, L.; Klepka, A.; Staszewski, W.; Aymerich, F.; Uhl, T. Damage imaging in composites using nonlinear vibro-acoustic wave modulations. *Struct. Control Health Monit.* **2018**, *25*, e2063. [CrossRef]
5. Xiao, C.; Zheng, H.; Hu, L.; Wang, Y.; Cao, Y. Study of micro-crack localization based on vibro-acoustic modulation. *J. Phys. Conf. Ser.* **2018**, *1074*, 012069. [CrossRef]
6. Aslam, M.; Bijudas, C.R.; Nagarajan, P.; Remanan, M. Numerical and Experimental Investigation of Nonlinear Lamb Wave Mixing at Low Frequency. *J. Aerosp. Eng.* **2020**, *33*, 04020037. [CrossRef]
7. Bazrafkan, M.M.; Rutner, M. Defect Localization in Metal Plates Using Vibroacoustic Modulation. *NDT* **2023**, *1*, 3–21. [CrossRef]
8. Klepkal, F.A.A.; Staszewski, W.J.; Uhl, T. Nonlinear vibro-acoustic wave modulations for impact damage detection in composites. In Proceedings of the 15th European Conference on Composite Materials, Venice, Italy, 24–28 June 2012.
9. Lim, H.J.; Sohn, H. Necessary Conditions for Nonlinear Ultrasonic Modulation Generation Given a Localized Fatigue Crack in a Plate-Like Structure. *Materials* **2017**, *10*, 248. [CrossRef] [PubMed]
10. Dorendorf, L.; Lalkovski, N.; Rutner, M. Physical explanation for vibro-acoustic modulation due to local and global nonlinearities in a structure and its experimental and numerical validation. *J. Sound Vib.* **2022**, *528*, 116885. [CrossRef]
11. Dorendorf, L.; Lalkovski, N.; Boll, B.; Rutner, M. Separation and quantification of damage-induced and non-damage-induced vibro-acoustic modulation and the problem of contrary modulations. *Mech. Syst. Signal Process.* **2025**, *232*, 112708. [CrossRef]
12. Boll, B.; Dorendorf, L.; Oppermann, P.; Willmann, E.; Fiedler, B.; Renner, B.-C.; Rutner, M.; Meißner, R.H. Synthetic generation of vibroacoustic modulation signals for structural health monitoring. *Mech. Syst. Signal Process.* **2023**, *200*, 110498. [CrossRef]
13. Donskoy, D.; Sutin, A.; Ekimov, A. Nonlinear acoustic interaction on contact interfaces and its use for nondestructive testing. *NDT E Int.* **2001**, *34*, 231–238. [CrossRef]
14. Duffour, P.; Morbidini, M.; Cawley, P. A study of the vibro-acoustic modulation technique for the detection of cracks in metals. *J. Acoust. Soc. Am.* **2006**, *119*, 1463–1475. [CrossRef]
15. Donskoy, D.M. Nonlinear Acoustic Methods. In *Encyclopedia of Structural Health Monitoring*; John Wiley & Sons, Ltd.: Hoboken, NJ, USA, 2009. [CrossRef]
16. Aymerich, F.; Staszewski, W.J. Experimental Study of Impact-Damage Detection in Composite Laminates using a Cross-Modulation Vibro-Acoustic Technique. *Struct. Health Monit.* **2010**, *9*, 541–553. [CrossRef]
17. Hu, H.F.; Staszewski, W.J.; Hu, N.Q.; Jenal, R.B.; Qin, G.J. Crack detection using nonlinear acoustics and piezoceramic transducers—Instantaneous amplitude and frequency analysis. *Smart Mater. Struct.* **2010**, *19*, 065017. [CrossRef]
18. Donskoy, D.M.; Ramezani, M. Separation of amplitude and frequency modulations in Vibro-Acoustic Modulation Nondestructive Testing Method. *Proc. Meet. Acoust.* **2018**, *34*, 045002. [CrossRef]
19. Donskoy, D.; Golchinfar, B.; Ramezani, M.; Rutner, M.; Hassiotis, S. Vibro-acoustic amplitude and frequency modulations during fatigue damage evolution. *AIP Conf. Proc.* **2019**, *2102*, 040004. [CrossRef]
20. Klepka, A.; Dziedziech, K.; Mrówka, J.; Górski, J. Experimental investigation of modulation effects for contact-type interfaces in vibro-acoustic modulation tests. *Struct. Health Monit.* **2021**, *20*, 917–930. [CrossRef]
21. Oppermann, P.; Dorendorf, L.; Rutner, M.; Renner, C. Nonlinear modulation with low-power sensor networks using undersampling. *Struct. Health Monit.* **2021**, *20*, 3252–3264. [CrossRef]
22. Gorski, J.; Dziedziech, K.; Klepka, A. Experimental investigation of modulation types in modulation transfer tests. *Mech. Syst. Signal Process.* **2023**, *200*, 110589. [CrossRef]
23. Klepka, A.; Staszewski, W.; Jenal, R.; Szwedo, M.; Iwaniec, J.; Uhl, T. Nonlinear acoustics for fatigue crack detection—Experimental investigations of vibro-acoustic wave modulations. *Struct. Health Monit.* **2012**, *11*, 197–211. [CrossRef]
24. Klepka, A.; Dziedziech, K. Vibro-acoustic modulation for damage detection -investigation of nonlinear effects for contact-type damage. In Proceedings of the International NDT Conference & Exhibition, Singapore, 27–28 February 2025. [CrossRef]

25. Haykin, S. *Communication Systems*, 4th ed.; Wiley India Pvt. Limited: Delhi, India, 2006.
26. Lathi, B.P.; Ding, Z. *Modern Digital and Analog Communication Systems*; Oxford University Press: Oxford, UK, 2010.
27. Donskoy, D.; Liu, D. Vibro-acoustic modulation baseline-free non-destructive testing. *J. Sound Vib.* **2021**, *492*, 115808. [CrossRef]
28. Donskoy, D.; Zagrai, A.; Chudnovsky, A.; Golovin, E.; Agarwala, V. Nonlinear vibro-acoustic modulation technique for life prediction of aging aircraft components. In Proceedings of the 3rd European Workshop—Structural Health Monitoring, Granada, Spain, 5–7 July 2006; Volume 2006, pp. 251–258. Available online: https://www.scopus.com/pages/publications/66749171931 (accessed on 5 January 2026).